Lawrence Berkeley National Laboratory

Title

CO2 gas/oil ratio prediction in a multi-component reservoir by combined seismic and electromagnetic imaging

Permalink

https://escholarship.org/uc/item/0d65c9b1

Authors

Hoversten, G.M.
Gritto, Roland
Washbourne, John
et al.

Publication Date

2002-08-28

Peer reviewed

CO_2 Gas/Oil Ratio Prediction in a Multi-Component Reservoir by Combined Seismic and Electromagnetic Imaging

G. M. Hoversten [1]
Roland Gritto [1]
John Washbourne [2]
Tom Daley [1]

1 Lawrence Berkeley National Laboratory
2 TomoSeis Inc.

Abstract

Crosswell seismic and electromagnetic data sets taken before and during CO_2 flooding of an oil reservoir are inverted to produce crosswell images of the change in compressional velocity, shear velocity and electrical conductivity during a CO_2 injection pilot study. A rock properties model is developed using measured log porosity, fluid saturations, pressure, temperature, bulk density, sonic velocity and electrical conductivity. The parameters of the rock properties model are found by an L1-norm simplex minimization of predicted and observed compressional velocity and density. A separate minimization using Archie's law provides parameters for modeling the relations between water saturation, porosity and the electrical conductivity. The rock properties model is used to generate relationships between changes in geophysical parameters and changes in reservoir parameters. The electrical conductivity changes are directly mapped to changes in water saturation. The estimated changes in water saturation are used with the observed changes in shear wave velocity to predict changes in reservoir pressure. The estimation of the spatial extent and amount of CO_2 relies on first removing the effects of the water saturation and pressure changes from the observed compressional velocity changes, producing a residual compressional velocity change. The residual compressional velocity change is then interpreted in terms of increases in the CO_2/oil ratio. Resulting images of CO_2/oil ratio show CO_2 rich zones that are well correlated with the location of injection perforations with the size of these zones also correlating to the amount of injected CO_2. The images produced by this process are better correlated to the location and amount of injected CO_2 than are any of the individual images of change in geophysical parameters.

Introduction

Crosswell seismic and electromagnetic technology has been developed over the past two decades to provide high spatial resolution images of the seismic velocities (P and S) and the electrical conductivity of the inter-well region. The majority of effort, as measured by the topics of published and presented work, has concentrated on developing and improving algorithms for estimating the geophysical parameters themselves (Newman 1995, Lazaratoz et al. 1995, Wilt et al 1995, Nemeth et al. 1997, Goudswaard et al. 1998 to list but a few). In most applications where nongeophysical parameters such as temperature during steam flood (Lee et al. 1995) or CO_2 saturations during CO_2 flood (Harris et al. 1995, Wang et al. 1998) are the object of the crosswell survey, correlations

1

between the geophysical parameters, velocity or electrical conductivity, and the desired reservoir parameter are derived and used to infer the distribution of reservoir parameters from the distribution of the geophysical parameters. The output from the survey is still most commonly a cross section of velocity, electrical conductivity or the time-lapse change of these parameters, which is then discussed in terms of its implications for the distribution and/or change of the parameter of interest (temperature, CO_2 saturation, etc.).

The simple extension of this is to use the parameter relationships (e.g. a regression fit between velocity and temperature) to convert a geophysical parameter to a reservoir parameter image. This approach can be used successfully in relatively simple reservoir systems with a minimum of fluid components and/or spatial variations in other controlling parameters (such as porosity, pressure, and temperature). However, in many settings the geophysical parameters depend on many reservoir parameters that are variable in both space and time. In particular, porosity, pressure, water and gas saturation strongly influence seismic velocity. Electrical conductivity can generally be described as a function of porosity, water saturation, and fluid conductivity (Archie 1942), although clay content may also need to be considered. As we will show, in a complex reservoir fluid system, the spatial distribution of the time-lapse change in geophysical parameters, such as velocity, can vary significantly from the spatial distribution of the time-lapse change in a desired reservoir parameter, such as CO_2 saturation in oil. This difference results from the dependence of the geophysical parameters on more than one reservoir parameter such as pressure and water saturation. These multiple dependencies must be sorted out before a picture of any single reservoir parameter can be obtained.

It has become common practice to use time-lapse changes in compressional and shear impedance mapped at the top of a reservoir to calculate time-lapse changes in effective pressure and water saturation within the reservoir without significant gas saturations (Landro 2001). However, in systems where natural gas is present in significant concentrations or where gas in the form of CO_2 is introduced, quantitative prediction of pressure and fluid saturation changes becomes problematic because of trade-offs in the effects of the multiple reservoir parameters on the mapped geophysical parameters. The situation is further complicated if the objective is to monitor CO_2 injection into a reservoir already containing natural gas in addition to oil and water.

The objective of the work described in this paper is to demonstrate a methodology of combining time-lapse changes in electric conductivity, compressional and shear wave velocity with a detailed rock properties model to produce quantitative estimates of the change in fluid saturations (including oil, water and gas) and reservoir pressure.
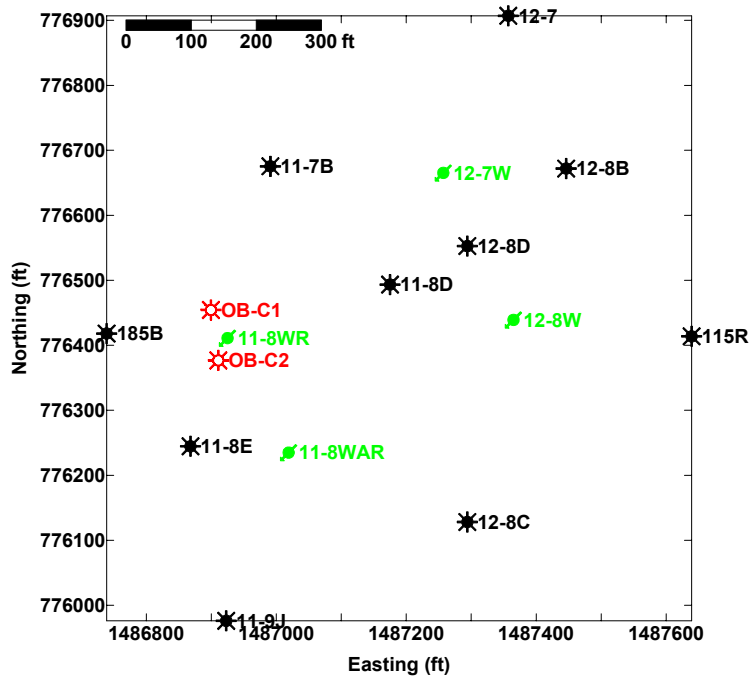
The Field Experiment

Crosswell seismic tomography and electromagnetic imaging have been demonstrated in separate applications over the last decade. The SEG special issue "Crosswell Methods" (Rector, 1995) contains several papers on the application of crosswell seismic tomography specifically for thermal process monitoring and several others on crosswell

EM monitoring of water floods. In addition, Wilt et al. (1997) report on the application of crosswell EM in steam flood monitoring.

We have conducted crosswell seismic and electromagnetic (EM) measurements in the Lost Hills oil field in southern California during a CO_2 injection pilot study conducted by Chevron Petroleum Co. The objective of the pilot was to demonstrate enhanced oil recovery resulting from CO_2 injection. We have used the opportunity to study geophysical imaging of the reservoir during CO_2 injection.

The portion of the Lost Hills field where this experiment took place has been undergoing water flood since 1995. The CO_2 pilot covers four injection wells and surrounding producers. Figure 1 shows the well placement in the affected portion of the field. The observation wells, OB-C1 and OB-C2, were drilled for the pilot and fiberglass-cased to enable the use of crosswell EM. The nearby CO_2 injector (11-8WR) is located 20 feet out of the crosswell-imaging plane. The injection wells are hydraulically fractured (hydro-frac) to increase injectivity into the low-permeability diatomite reservoir. In some cases, downhole pressures were increased above the lithostatic pressure, which may have induced fracturing above the desired injection interval. If the fracture did indeed extend above the desired interval, much of the injected CO_2 would likely not sweep its intended target, but rather move in to the higher section.

Figure 1. *Area of the Lost Hills field affected by CO_2 injection. Four water injectors (shown in green) were converted to CO_2 injection in September 2000. The crosswell experiments took place between observation wells OB-C1 and OB-C2 (shown in red). A flow simulation production history match was done on the portion of the field covered by this figure.*

The baseline crosswell seismic and EM surveys were conducted in September 2000, just prior to the beginning of CO_2 injection. A second EM survey was conducted in mid April 2001, and a second seismic survey was conducted in May 2001. In addition to the crosswell surveys, the two observation wells OB-C1 and OB-C2 were relogged for electrical resistivity in January 2001.

A Rock-Properties Model

The reservoir parameters that have a dominant affect on geophysical parameters are porosity, pressure, fluid saturation and the amount of dissolved hydrocarbon gas or CO_2 in oil. Pressure has a significant effect in Lost Hills because this is a shallow reservoir in soft rock. Conversion of geophysical images of the inter-well region to reservoir parameters requires a rock-properties model relating the geophysical parameters to the reservoir parameters. We sought a model that would be able to predict observed velocity, density and electrical conductivity from observed pressure, porosity and fluid saturations. Laboratory measurements of the dry frame moduli and grain density of the Diatomite reservoir rock were unavailable, so to compute the seismic velocity we have used the Hertz-Mindlin contact theory for the effective bulk (K_{dry}) and shear (G_{dry}) moduli of a dry dense random pack of spherical grains given by the following expressions.

$$K_{dry} = \left[\frac{n^2 (1-\phi_0)^2 G^2}{18\pi^2 (1-v)^2} \cdot P \right]^{1/3} \qquad (1)$$

$$G_{dry} = \frac{5-4v}{5(2-v)} \left[\frac{3n^2 (1-\phi_0)^2 G^2}{2\pi^2 (1-v)^2} P \right]^{1/3} \qquad (2)$$

where P is the pore pressure, v is the grain Poisson's ratio, G is the grain shear modulus and n is the average number of other grains each grain contacts.

Equations (1) and (2) describe the effective dry frame moduli at critical porosity ϕ_0. The modified Hashin-Strikman (Hashin & Shtrikman 1963) lower bound given by Dvorkin and Nur (1996)

$$K_{eff} = \left[\frac{\phi/\phi_0}{K_{dry} + 4/3G_{dry}} + \frac{1-\phi/\phi_0}{K + 4/3G_{dry}} \right]^{-1} - 4/3G_{dry} \qquad (3)$$

$$G_{eff} = \left[\frac{\phi/\phi_0}{G_{dry} + \frac{G_{dry}}{6}\left(\frac{9K_{dry} + 8G_{dry}}{K_{dry} + 2G_{dry}}\right)} + \frac{1 - \phi/\phi_0}{G + \frac{G_{dry}}{6}\left(\frac{9K_{dry} + 8G_{dry}}{K_{dry} + 2G_{dry}}\right)} \right]^{-1}$$

(4)

$$- \frac{G_{dry}}{6}\left(\frac{9K_{dry} + 8G_{dry}}{K_{dry} + 2G_{dry}}\right)$$

is used to model the dry frame moduli (K_{eff} and G_{eff}) at porosity ϕ, where K is the grain bulk modulus.

The bulk modulus of the fluid saturated rock (K_{sat}) is modeled by Gassmann's equation (Gassmann 1951)

$$K_{sat} = K_{grain}\left[\frac{\phi \cdot K_{eff} - \left[\frac{(1+\phi) \cdot K_{fluid} \cdot K_{eff}}{K_{grain}}\right] + K_{fluid}}{(1+\phi) \cdot K_{fluid} + \phi \cdot K_{grain} - \left[\frac{K_{fluid} \cdot K_{eff}}{K_{grain}}\right]} \right]$$

(5)

where K_{fluid} is the aggregate bulk modulus of the fluids filling the pore space.

The possible fluids filling the pore space are oil, brine, hydrocarbon gas and CO_2. A common approach for calculating K_{fluid} is to use Wood's mixing la:

$$1/K_{fluid} = S_w/K_{brine} + S_{oil}/K_{oil} + S_{hcg}/K_{hcg} + S_{co2}/K_{co2}$$ (6)

where the water saturation (S_w), oil saturation (S_{oil}), hydrocarbon gas saturation (S_{hcg}) and CO_2 saturation (S_{co2}) sum to 1.0. We will discuss this method of calculating K_{fluid} at the end of this section.

The bulk density is given by a simple mixing law

$$\rho_{bulk} = (1-\phi)\rho_{grain} + \phi\left(1 - S_{hcg} - S_w - S_{CO_2}\right)\rho_{oil} +$$

$$\phi S_w \rho_{brine} + \phi S_{hcg} \rho_{gas} + \phi S_{CO_2} \rho_{CO_2}$$

(7)

where ρ_{grain}, ρ_{oil}, ρ_{brine} and ρ_{CO_2} are the grain, oil, gas and CO_2 densities respectively as a function of pressure and temperature.

The fluid bulk moduli $K_{brine}, K_{oil}, K_{gas}$ and densities ρ_{brine}, ρ_{oil}, ρ_{gas} of the brine, oil, and hydrocarbon gas respectively are computed using relations from Betzel and Wang (1992). The bulk modulus and density of CO_2, K_{CO_2} and ρ_{CO_2}, respectively, as well as the moduli and densities of CO_2-hydrocarbon gas mixtures are modeled using relations from Magee and Howley (1994).

The bulk electrical conductivity (σ_{bulk}) of the reservoir rock is modeled using Archie's (1942) relationship

$$\sigma_{bulk} = \sigma_{brine} \cdot \phi^m \cdot S_w^n \tag{8}$$

where σ_{brine} is the fluid conductivity.
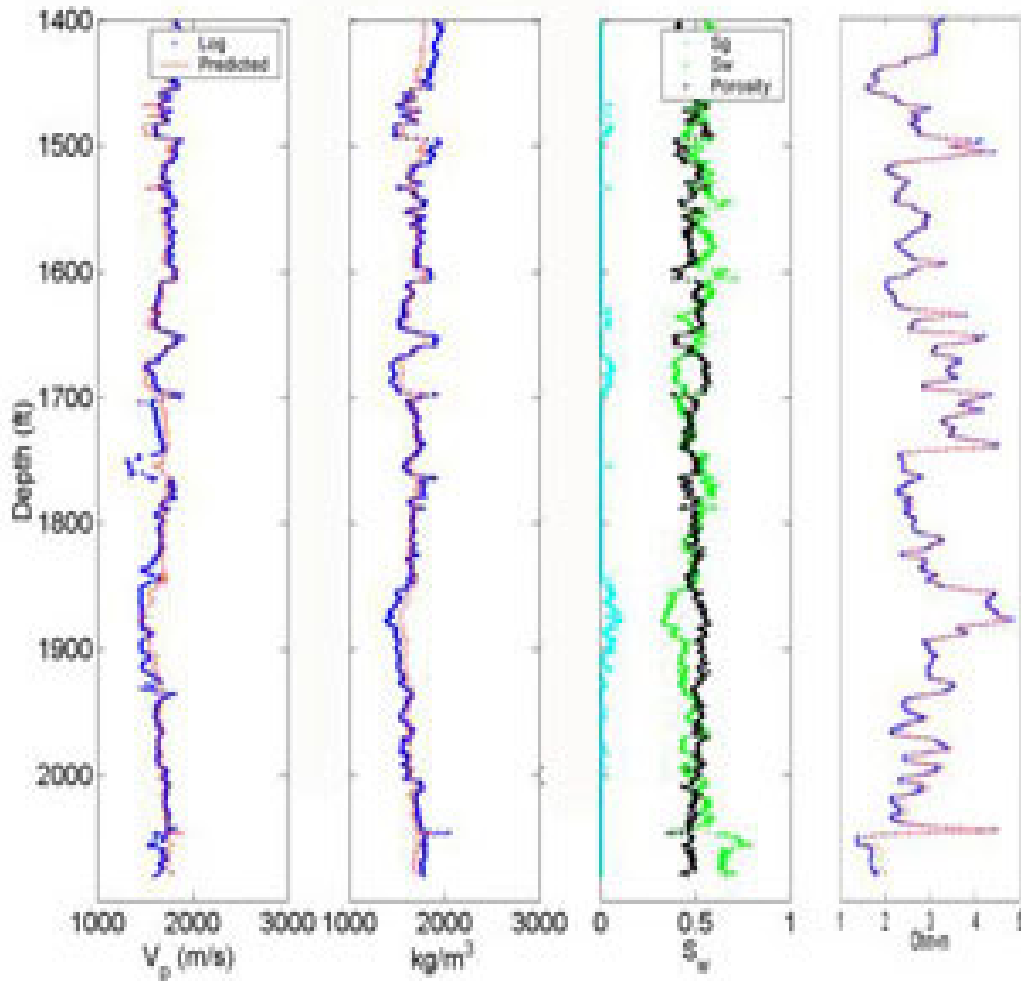
Figure 2. *Rock properties model uses logged porosity (black), water saturation (green) and gas saturation (light blue) as inputs in a multiparameter regression to predict the velocity (left panel), density (second from left panel) and electrical resistivity (right panel). Measured velocity, density, and resistivity are shown in blue; model predicted values are shown in red.*

The model parameters in Equations (1) through (7) were found by using a simplex algorithm to minimize the combined misfit between observed and predicted compressional velocity (V_p) and density, given the ϕ, S_w and S_{hcg} logs. Because the observation wells used in the crosswell surveys did not have full logging suites, a nearby well with a full suite of logs was used. The parameters in (8) were determined by a regression using the OB-C1 σ, ϕ, and S_w logs. The predicted V_p, ρ, and $1/\sigma$ compared to the observed logs are shown in Figure 2, with the model parameters determined from the regressions listed in Table 1.

Table 1: *Rock properties model parameters by model constituent. Model parameters fixed in the regression of well log data are shown in bold type. Asterisk (*) indicates that lithostatic pressure was calculated as a function of depth using the integrated density log, and pore pressure was taken as hydrostatic. Effective Pressure = Lithostatic – Hydrostatic Pressure*

	Dry Frame Modulus	Gassmann's fluid substitution	Fluids	Electrical Conductivity	Regression Values
Grain Shear Modulus	x				17.84
Grain Poisson Ratio	x				0.107
Grain Density	x	Dry Rock			2.358 (g/cc)
# of contacts/grain	x	K			3.68
Effective Pressure	x				*
Critical Porosity	x				**0.55**
Pore Pressure			x		*
Oil API gravity			x		**21.7**
Gas Density ratio (G)		Fluid K	x		0.585
Brine Salinity			x		**0.023**
Temperature			x		**42(C)**
Fluid conductivity				x	0.23 (S/m)
Porosity exponent				x	-1.66
Water Saturation exponent				x	-1.85
Gas correction		x			0.0068943

*   Litostatic Pressure from integrated density logs, Eff. P = Litho - Hydro static

Parameters listed in bold type in Table 1 (critical porosity, oil API gravity, brine salinity and temperature) were held fixed in the regression. These values, with the exception of critical porosity, came from direct measurement. Although we are not interested in the model parameters *per se* (we are only interested in the models ability to predict V_p, V_s and ρ, given reservoir parameters), note that their values are quite realistic. The gas density G is very close to that of methane. Estimated shear modulus and grain density of the diatomite grains is very close to the values of 18 (GPa) and 2.3 g/cc estimated by Wang (2001). Bilodeau (1995) measured an average grain density of 2.37 g/cc from another location in the diatomite at Lost Hills, he also measured -1.84, -1.95 and 0.21 for Archie's Law porosity exponent, saturation exponent and fluid conductivity, respectively on the same samples. The critical porosity used is much higher than for

average sedimentary rock, but is consistent with the porosity range of 50-70% in diatomite.

In Table 1, only one parameter, "gas correction", is listed under the Gassmann fluid substitution column. In addition, the Gassmann formula uses the dry frame modulus as well as the fluid bulk moduli derived from the Betzel and Wang (1992) relations. However, we found that to fit the observed velocity in areas where the gas saturation was non-zero, the gas effect had to be reduced. The overestimation of the gas effect on fluid bulk modulus by the Wood's mixing law, Equation (6), has been observed by Brie et al. (1995). A better match between predicted and observed velocity could be achieved by a simple correction to the gas term in (6), yielding a modified equation

$$K_{fluid} = 1.0 / \begin{bmatrix} G_c * (S_{hcg} / K_g) + (S_w / K_w) + \\ ((1 - S_{hcg} - S_w - S_{c02}) / K_o) + (S_{co2} / K_{co2}) \end{bmatrix} \tag{9}$$

where G_c is the gas correction listed in Table 1.

The pressure prediction capability of the model was validated by comparison to measurements made by Wang (2001) on core samples of diatomite from Lost Hills. Figure 3 shows the measured compressional velocity for vertical and horizontal propagation. These measurements show a horizontal-to-vertical velocity anisotropy of 1.047 that varies slightly as a function of pressure. We will come back to the velocity anisotropy when we consider the velocity inversion of the crosswell data.
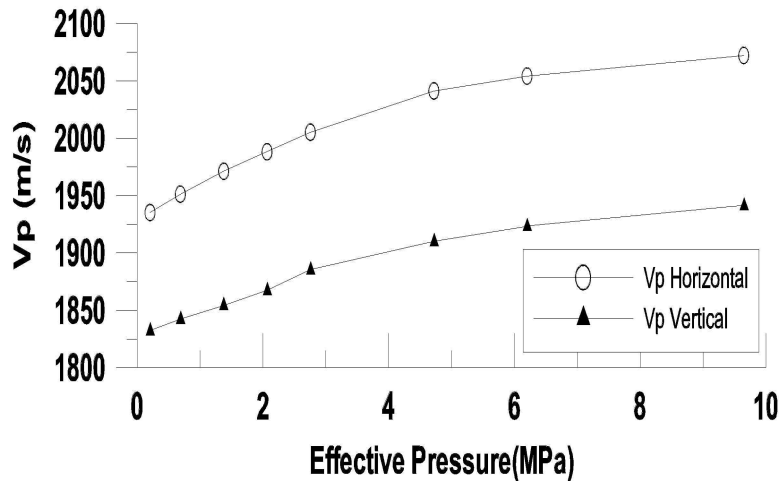
Figure 3 *Vertical and horizontal compressional velocity as a function of effective pressure measured on Lost Hills Diatomite core by Wang (2001). Core was saturated with 19 API oil and 200,000 ppm brine (50-50 ratio) at 22.7 C.*

Figure 4 presents the data from Figure 3 recast as velocity changes as a function of pressure changes at a reference pressure of 4.7 MPa, the average effective pressure in the reservoir at the start of CO_2 injection. For expected decreases in effective pressure

(increases in pore pressure) in the range 0 to 3 MPa from the reference pressure the rock properties model predictions are within a few percent of the lab measurements for vertical velocity. The rock properties model is derived from log sonic measurements that are dominated by vertical propagation along the borehole, so the correspondence to the vertical core measurements is expected. For changes in pressure above the reference pressure the lab measurements show a change in the slope of the curve, with the quality of the fit between model and lab data decreasing. The difference in this region is probably associated with pore crushing in the lab samples that is not accounted for in the rock properties model.
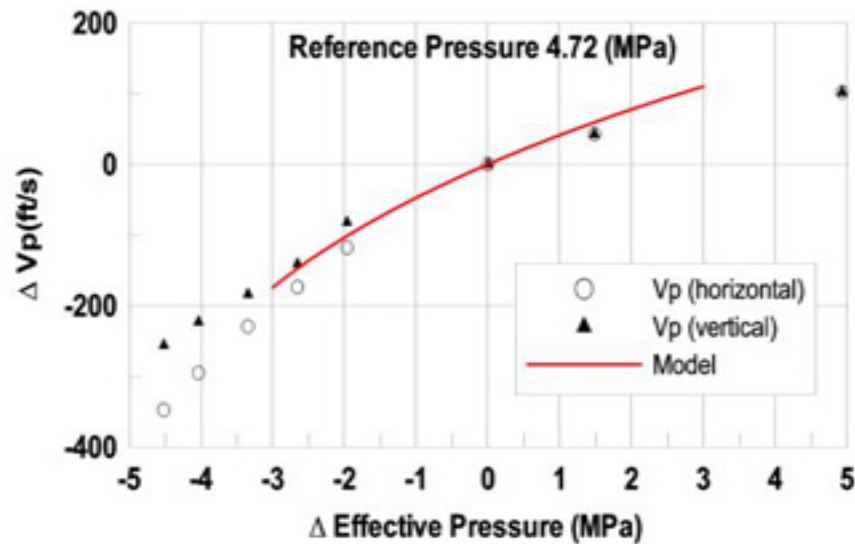

Figure 4 *Predicted velocity change as a function of change in effective pressure compared to laboratory measurements on Lost Hills diatomite core samples.*

The model described by Equations (1) – (5) and (7) – (9), with constants listed in Table 1, is used to calculate time-lapse changes in reservoir parameters, given estimates of the time-lapse changes in geophysical parameters derived from inversion of the observed geophysical data, as described in the following sections.

Integrated TimeLapse Geophysical Images

The algorithms, assumptions, starting models, and amount of incorporated *a priori* information all greatly affect the resulting inverse velocity and conductivity models. Inversions of the individual data sets done separately without any mechanism for linking the models, produces inverse images of V_p, V_s and σ with little spatial correlation. Since we assume that the changes in reservoir parameters affect all of the geophysical parameters, albeit in different ways, we expect a certain degree of spatial correlation between changes in the different geophysical parameters. This assumption acts as a form of constraint on the possible solutions. In this experiment, sonic logs were not run in OB-C1 or OB-C2, but conductivity logs were run in both wells. The strategy we adopted to maximize the spatial correlation between velocity and conductivity inverse images was to

begin with the EM data, where the most *a priori* information existed and then use the conductivity images to produce starting V_p models, followed by producing a starting V_s model from the final V_p model. The conductivity logs were used to build starting models
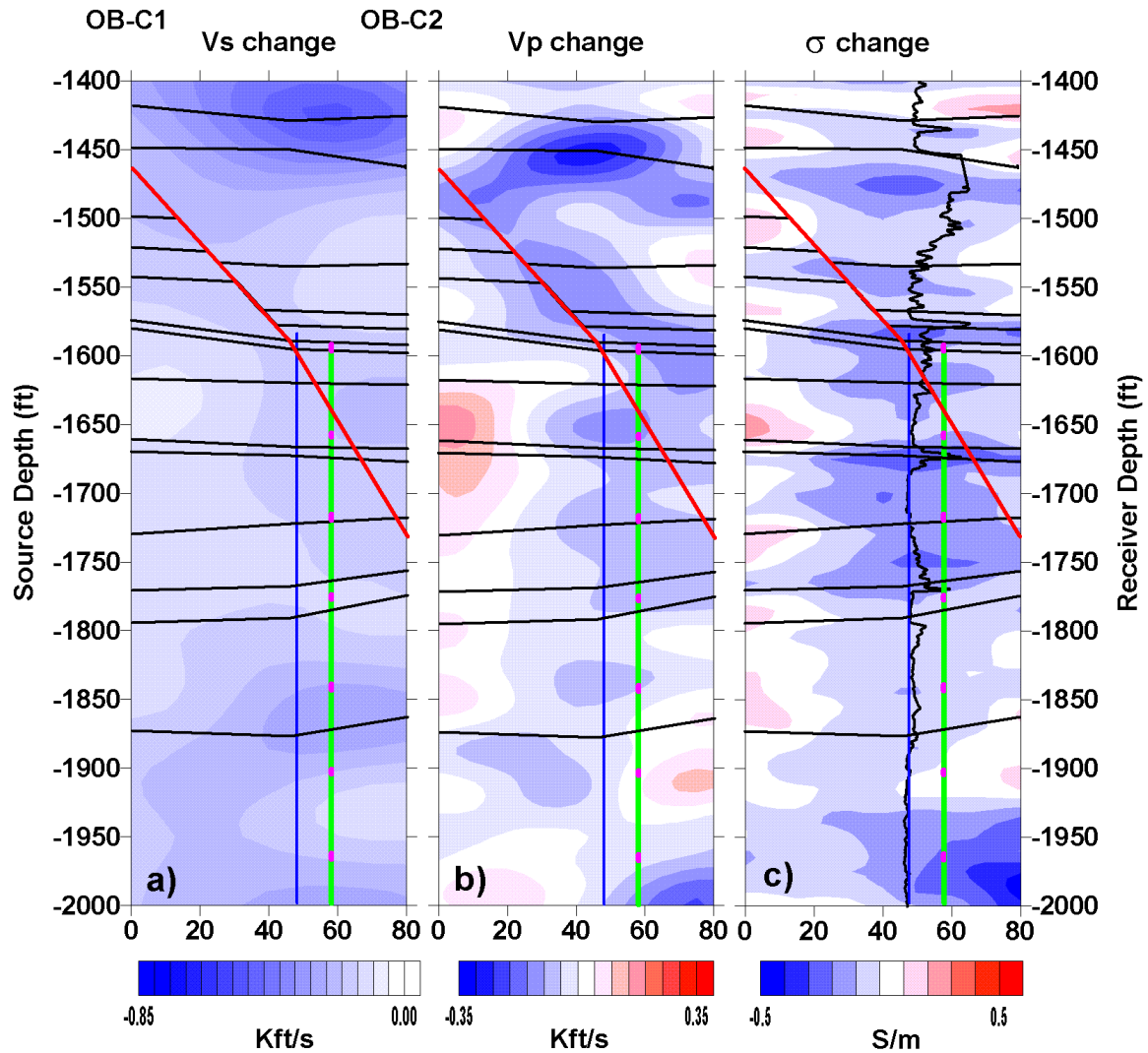
Figure 5. *Time-lapse changes in (a) shear velocity, (b) compressional velocity and (c) electrical conductivity. The EM images were used to construct starting models for the V_p inversions; the resulting V_p images were used to construct starting models for the V_s inversions. Major unit boundaries are shown as black horizontal lines, estimated location of previous water injection fracture is shown as vertical blue line, estimated location of the CO_2 injection fracture is shown as a vertical green line, perforation intervals for CO_2 injection are shown as magenta dots, mapped location of a fault zone is shown as the red diagonal line. The permeability log in the out-of-plane CO_2 injection well (11-8WR) is shown in black on panel (c).*

for the EM inversions. (The EM inversion algorithm is described by Newman [1995]). We chose to use the conjugate gradient algorithm of Jackson and Tweeton (1996) for the

10

travel-time tomography because, unlike a SIRT algorithm, the final model is sensitive to the initial model and is perturbed from the starting model only as much as needed to fit the observed data.

The EM inversion for the data at initial conditions (late August 2000 before CO_2 injection) was started from a model built by laterally interpolating the conductivity logs between the OB-C1 and OB-C2 wells. The final inversion model from this data was then used as the starting model for the inversion of the April 2001 data. The difference of the two inversions provides the time-lapse change in conductivity shown in Figure 5(c). A high degree of correlation exists between the permeability log from the injector and the areas where the largest decrease in conductivity occur. The correlation between high permeability and large changes in conductivity (water saturation) is expected. Also, the largest σ changes occur more in alignment with the estimated location of the previous water injection fracture than with the much newer CO_2 fracture. This finding is not surprising when we consider that water injection was ongoing for more that 6 years and thus likely produced a high-permeability damage zone that is a better conduit to flow than the very new CO_2 fracture.

Next, the conductivity models from the two inversions were converted to compressional velocity, using the rock-properties model described earlier. These were then used as initial models in the inversion of the V_p travel-time data to produce the change in V_p shown in Figure 5(b). In addition to velocity changes occurring in the vicinity of the estimated water injection fracture location, there are decreases in V_p that align with the upper section of the mapped fault. Since there are little conductivity changes are associated with the fault, indicates that pressure changes are occurring along the fault zone without significant changes in water saturation. Both the conductivity and V_p change sections (Figure 5(c) and (b)) show an increase in conductivity and V_p near the OB-C1 and OB-C2 wells. This is caused by an increase in water saturation, as shown in the relogging of the wells in January 2001. The outward movement of water away from the injector well as CO_2 is injected causes a "rind" of increased S_w surrounding a volume affected by CO_2. The volume of rock affected by CO_2 injection will have reduced water content as either CO_2 fills the pore space or oil absorbs CO_2 and swells, expelling water. This volume will have a surrounding "rind" of increased water saturation.

The algorithm (Jackson & Tweeton 1996) used to produce the velocity tomograms shown in Figure 5 allows setting a constant velocity anisotropy and a constant dip of the anisotropy symmetry axis for the entire cross section. Values of the horizontal/vertical velocity and the dip of the symmetry axis were varied between 0.9 and 1.1 and –10 to +10, respectively, in a series of tomographic inversions. The final values of 1.05 and 7 degrees from vertical (respectively) used in Figure 5 produced the flattest travel time misfit versus ray angle scatter plot with the minimum RMS data misfit. Figure 6(a) shows the travel time residual plot for a V_p model without anisotropy and Figure 6(b) shows the residual for the final V_p model shown in Figure 5(b). The horizontal to vertical velocity ratio of 1.05 from the crosswell seismic tomograms compares remarkably well to the value of 1.047 from core measurements shown earlier in Figure 3. In addition, the structural dip of the reservoir units in the plane of the crosswell experiment is 7 degrees.
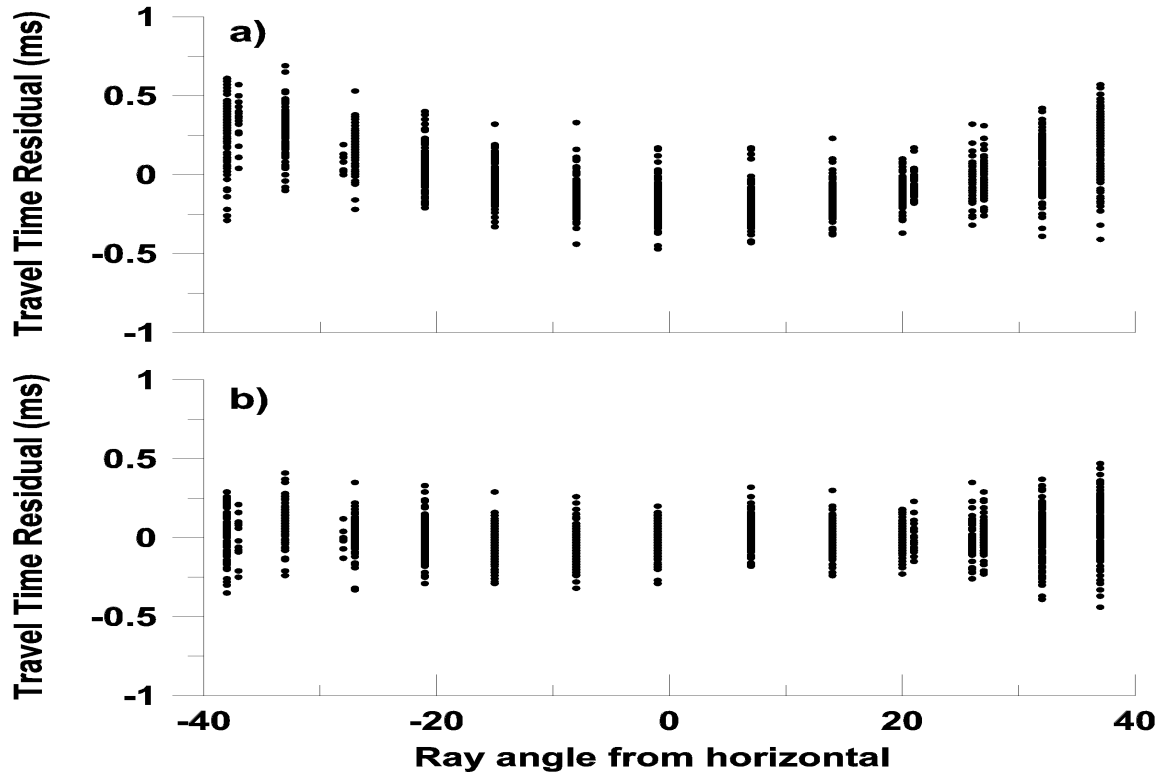
Figure 6. *Travel time residual (observed – calculated) vs. ray angle from horizontal. Panel (a): homogeneous halfspace starting model with no anisotropy or dip of the velocity field. Panel (b): homogeneous halfspace starting model with $V_{horizontal}/V_{vertical} = 1.05$ and symmetry axis 7 degrees from vertical.*

The starting models for the V_s inversions were converted from the final V_p sections using a V_p/V_s ratio derived from the rock properties model. The final V_s models were differenced to produce the change in V_s section shown in Figure 5(a). The V_s change section is much smoother that either the conductivity or V_p change sections. This results partially from the lower frequency content in the shear-wave data. The shear-wave data was acquired using an orbital vibrator source with a center frequency of 500 Hz, whereas the compressional wave data was acquired using a piezoelectric source with a center frequency of 2000 Hz. The V_s change section is also smoother because the V_s is relatively insensitive to changes in water saturation that have high spatial variability and more sensitive to pressure changes that have much lower spatial variability. Even with the smoother spatial changes in V_s we see a correlation with V_p and conductivity changes. In particular the zone along the fault shows a decrease in V_s, lending support to our interpretation that pressure is changing along the fault zone.

The Effects of Gas on Seismic Velocity and Density

The goal is to predict changes (Δ) in reservoir pressure, fluid saturations, and the amount of absorbed CO_2 in the oil as the CO_2 flood proceeds. We assume that the porosity remains constant over the time of the experiment. To use the rock-properties model to predict the changes in reservoir parameters from the changes in geophysical

parameters, we must define certain values for reference parameters to compute changes about. In particular, reference water saturation (S_w) and porosity (ϕ) of 0.5 and 0.52 respectively, are taken from the averages in the OB-C1 well over the reservoir interval prior to CO_2 injection. The reference pore pressure (P_{pore}) is taken from a history matched flow simulation model at the beginning of CO_2 injection. The reference effective pressure (P_{eff}) on the rock frame for seismic velocity calculations is calculated from the integrated density log minus P_{pore}. We will consider the sensitivity of our predictions to values of the reference parameters below.

Both hydrocarbon gas and CO_2 in the reservoir affect the seismic velocities through two possible mechanisms: first, by directly changing the bulk modulus of the composite fluid in the pore space as gas saturation changes (Equation 9) or second by changing the bulk modulus of the oil as the amount of dissolved gas changes. Equation (10), from Batzle & Wang (1992), gives the maximum amount of gas that can dissolve in oil expressed as a gas/oil ratio (R_G^{max}) as a function of pore pressure (P_{pore}), temperature in degrees Celsius (T), oil API gravity (API):

$$R_G^{max} = 2.03 G_{grav} \left[P_{pore} \exp(0.02878 API - 0.00377T \right]^{1.205} \quad (10)$$

and gas gravity (G_{grav}). The gas/oil ratio is the volume ratio of liberated gas to remaining oil at atmospheric pressure and 15.6° C. Batzle & Wang (1992) also provide formulas for computing the velocity and density of oils with dissolved gas, which we have used in our calculations. An increase in the amount of dissolved gas in the oil, as measured by R_G, decreases both the bulk modulus and density, and hence the velocity, of the oil.

Figures 7(a) and (c) show the calculated ΔV_p and ΔV_s using oil with the maximum amount of dissolved hydrocarbon gas as functions of ΔP and ΔS_w at a reference point (reservoir just prior to CO_2 injection) where S_w, S_{hcg}, ϕ, and P_{eff} are equal to 0.5, 0.0, 0.52 and 4.7 (MPa), respectively. When S_{hcg} is non-zero and free gas exists, the behavior of ΔV_p with ΔP and ΔS_w changes markedly. Figure 7(b) shows ΔV_p for the same reference values as Figure 7(a), but with $S_{hcg} = 0.02$. Equation (10) is used to compute the maximum amount of dissolved gas as a function of pressure. As P_{pore} increases above the reference pressure, R_G^{max} increases, and we assume that *in situ* gas will dissolve into the oil up to R_G^{max}. As the pressure decreases below the reference pore pressure, R_G^{max} decreases, and gas will come out of solution, thereby increasing S_{hcg} above its reference value. This behavior is shown in Figure 8. At the reference pressure $S_{hcg} = 0.02$, as P_{pore} increases ($-\Delta P_{eff}$), gas dissolves in the oil and S_{hcg} decreases until near ΔP_{eff} of -2 MPa, all of the gas has dissolved in the oil. If P_{pore} decreases ($+\Delta P_{eff}$), gas comes out of the oil and S_{hcg} increases. This increase in S_{hcg} with $+\Delta P_{eff}$ accounts for the sharp gradients in ΔV_p seen in the upper portion of Figure 7(a) and (b).
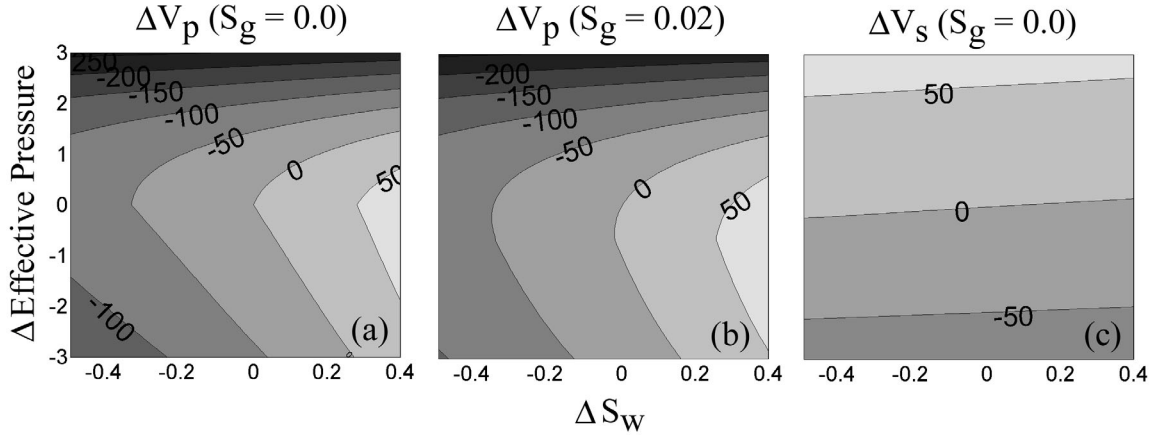
Figure 7. *Change in velocity (ft/s) as a function of change in effective pressure and water saturation at reference values of S_w=0.5, S_{hcg}=0.0, ϕ = 0.52 and P_{eff}=4.7MPa. Panel (a) ΔV_p (S_{hcg} = 0.0) (b) ΔV_p (S_{hcg} = 0.02) (c) ΔV_s (S_{hcg}=0.0). The oil contains the maximum amount of dissolved hydrocarbon gas as a function of pressure for the parameters of the rock properties model given in Table 1.*
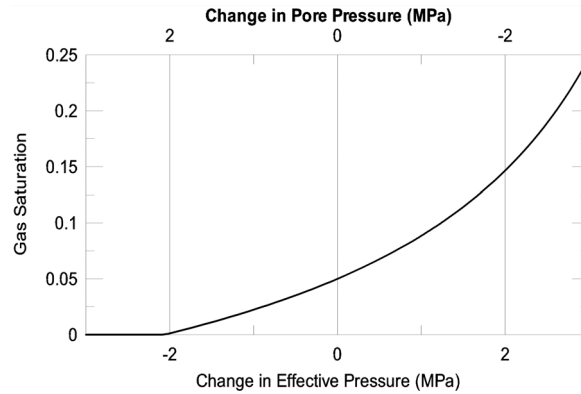
Figure 8. *Change in S_{hcg} as a function of pressure for the model calculations shown in Figure 12. Reference S_w=0.5, S_{hcg}=0.05, ϕ = 0.52 and P=4.7MPa.*

Although developed for hydrocarbon gas in oil, Equation (10) can be used to predict R_G^{max} for CO_2 if the appropriate gas gravity is used. Chung et al. (1988) present experimental results for CO_2 solubility in 22 API gravity oil at 66.7° C over a range of pressure. The predicted R_G^{max} from equation (10) using G=1.51 for CO_2, are within 1% of the measured values over the range of P_{pore} found in the Lost Hills reservoir, between 800 and 1,500 psi. Based on this comparison, use Equation (10) for both hydrocarbon gas and CO_2. Data from Chung et al. (1988) also show that the amount of CO_2 that will dissolve in oil, at the relatively low temperatures and pressures in our experiment, is independent of the amount of hydrocarbon gas already dissolved in the oil. We will make use of this fact later in our interpretation of the observed velocity changes.

The dissolution of gas into oil as P_{pore} increases produces two opposite effects on the composite fluid bulk modulus (Equation 9) and hence the bulk velocity of the rock An increase in P_{pore} causes R_G^{max} to increase, allowing more gas to dissolve in the oil,

14

lowering K_{oil}, which in turn reduces S_{hcg}. From Equation (9), we see a decrease in K_{oil} and in S_{hcg} act in opposition on K_{fluid}. When S_{hcg} is small, decreasing S_{hcg} to zero increased the bulk velocity of the rock more than lowering K_{oil} (by dissolving gas) decreases it, so that the net effect is to increase the bulk velocity of the rock.

Predicting Time-Lapse Changes in Reservoir Parameters

Before describing the process we have followed to estimate changes in fluid saturations, including *in situ* fluids and introduced CO_2, we acknowledge that the multitude of possible interactions between changes in pressure, hydrocarbon gas and CO_2, as well as the effects on the oil from dissolved gas components, is too large to be uniquely determined from our geophysical measurements. We propose a procedure that makes use of a number of (what we consider to be) reasonable and most probable assumptions to estimate the change in CO_2 gas/oil ratio, ΔR_{CO2}, and CO_2 saturation, ΔS_{CO2}. The most critical assumption, supported by field reservoir engineers and operations staff, is that introduced CO_2 will dissolve in oil almost immediately after injection. Thus, we treat changes in the CO_2 gas/oil ratio as the primary mechanism for velocity reduction after changes in S_w and P have been accounted for.

EM data provide an independent estimate of ΔS_w. Electrical conductivity (σ) is a much simpler function of reservoir parameters than is velocity and can be described by Archie's law (Archie 1942). Assuming ϕ is constant, $\Delta\sigma$ is only a function of ΔS_w and $\Delta\sigma_{brine}$. Because water flood had been in effect for over 6 years at the start of CO_2 injection, we assume σ_{brine} has reached equilibrium between injected and native water and does not change. Therefore, conductivity changes are interpreted solely in terms of water saturation changes.

The process of converting the geophysical Δ images to Δ reservoir parameters begins with predicting ΔS_w between the wells from the $\Delta\sigma$ image, assuming that ϕ and σ_{brine} are constant. The predicted ΔS_w is used with the observed ΔV_s and the relation illustrated in Figure 7(c) to predict ΔP. At this point, the predicted ΔS_w and ΔP sections have required only the assumption that $\Delta\sigma_{brine}$ does not change appreciably. Going beyond this point to use the observed ΔV_p with the predicted ΔS_w and ΔP to predict changes in CO_2 saturation along with changes in absorbed gases requires more assumptions and becomes riskier.

The predicted ΔS_w and ΔP are used to calculate the ΔV_p that results from ΔS_w and ΔP alone, assuming $S_{hcg}=0$. Over the majority of the image plane, ΔS_w is negative, with the exception of small zones in the rind of water saturation which increase (as noted earlier). Predicted ΔP is negative over the entire inter-well section, thus producing a $-\Delta V_p$. The residual change in velocity (ΔV_R), equal to the calculated ΔV_p minus the observed ΔV_p, was generated. We expect the injected CO_2 to decrease V_p in excess of the effects of ΔS_w and ΔP by dissolving CO_2 in oil and possibly producing $S_{co2} > 0$. On the other hand, a $+\Delta V_R$ can result if the assumption of no *in situ* hydrocarbon gas, $S_{hcg}=0$, is incorrect. This effect can be seen by comparing Figure 7(a) and 7(b) where the presence of hydrocarbon gas reduces the change in V_p associated with a given ΔS_w and ΔP. As a

consequence, a calculated ΔV_p assuming $S_{hcg} = 0$ when $S_{hcg} > 0$ yields a calculated ΔV_p that is too large and hence a $+\Delta V_R$. If *in situ* hydrocarbon gas is present and has been accounted for in the calculation of ΔV_R, $+\Delta V_R$ can result if S_{hcg} is reduced, because the P_{pore} increase causes hydrocarbon gas to dissolve in the oil.

The OB-C1 log shows the presence of hydrocarbon gas over certain intervals within the reservoir. We noted a strong correlation between depth intervals with a non-zero S_{hcg} and $+\Delta V_R$. Therefore, a two-step process was used to calculate ΔV_R. The first pass used $S_{hcg} = 0$ as described. Next, sections of the image with $+\Delta V_R$ were recalculated assuming $S_{hcg} = 0.02$ (the average non-zero S_{hcg} in the reservoir interval). After the second pass calculation of ΔV_R, many of the areas that had $+\Delta V_R$ after the first pass calculations became negative.

There are thus three regions of the ΔV_R section between the wells to interpret: (1) $S_{hcg} = 0$ and $\Delta V_R < 0$, (2) $S_{hcg} > 0$ and $\Delta V_R < 0$, and (3) $S_{hcg} > 0$ and $\Delta V_R > 0$. Regions of the crosswell section corresponding to $S_{hcg} = 0$ and $\Delta V_R < 0$ require an assumption about the partitioning of effects of free CO_2 and CO_2 dissolved in oil on $-\Delta V_R$. We chose to allow the maximum increase in R_{CO2}, as given by Equation (10), for the given ΔP_{pore} and ΔS_w. If the $+\Delta R_{CO2}$ does not completely account for the $-\Delta V_R$, then ΔS_{CO2} was calculated to account for the rest. For regions where $S_{hcg} > 0$ and $\Delta V_R < 0$, we assumed that the $+\Delta P_{pore}$ caused by injection would drive as much of the initial S_{hcg} into the oil as possible, followed by the same assumption about the partitioning of the $-\Delta V_R$ between $+\Delta R_{CO2}$ and ΔS_{CO2} as above. Regions where $S_{hcg} > 0$ and $\Delta V_R > 0$ were converted to $-\Delta S_{hcg}$.

Analysis shows that the oil is fully saturated with hydrocarbon gas. Therefore, we assume that the starting point for CO_2 absorption is oil with R_{hcg} at its maximum value for the given P and T. As noted earlier, R_{CO2} and R_{hcg} are essentially independent, so that the oil can absorb the amount of hydrocarbon gas and CO_2 up to their respective R_G^{max}, indicated by Equation (10). Because we lack an equation for calculating K_{oil} with two separate dissolved gasses, we have assumed that equation (11) is an adequate approximation of the bulk modulus of the oil.

$$K_{oil}^{co2+hcg} = K_{oil}^{dead} + \Delta K_{oil}^{co2} + \Delta K_{oil}^{hcg} \tag{11}$$

K_{oil}^{dead} is the oil bulk modulus without any gas, ΔK_{oil}^{co2} is the difference between K_{oil}^{dead} and the oil bulk modulus with CO_2 dissolved, and ΔK_{oil}^{hcg} is the difference between K_{oil}^{dead} and the oil bulk modulus with hydrocarbon gas dissolved.

Calculating $+\Delta R_{CO2}$ for regions where $\Delta V_R < 0$ is a simple linear interpolation between observed $-\Delta V_R$ and calculated $-\Delta V_R$ for a range of $+\Delta R_{CO2}$. If R_{CO2} reaches the maximum given by Equation (10) then the remaining observed $-\Delta V_R$ is used in a linear interpolation between calculated $-\Delta V_R$ over a range of $+\Delta S_{CO2}$ to calculate S_{CO2}.
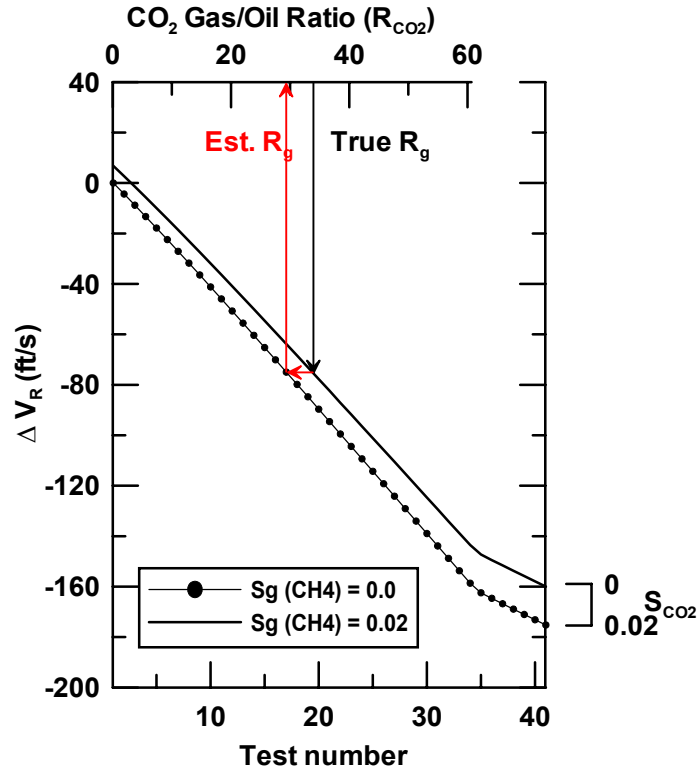
Figure 9. *ΔV_R as a function of R_{CO2} with and without hydrocarbon gas saturation, solid line is $S_{hcg}=0.02$, dotted line is $S_{hcg}=0.0$. The presence of S_{hcg} causes ΔV_R to be less negative than if $S_{hcg}=0.0$.*

The linear relation between ΔV_R and R_{CO2} is shown by the dotted line ($S_{hcg} = 0$) in Figure 9. In Figure 9, R_{CO2} increases from 0 to R_{CO2}^{max} from test number 1 to 34. From test number 34 to 41, S_{CO2} increases from 0 to 0.02, simulating the effect of progressively adding CO_2 that first dissolves in oil and after R_{CO2}^{max} is reached goes into the gas phase. Figure 9 also illustrates the effects of incorrectly assigning *in situ* hydrocarbon gas saturation. If $S_{hcg} > 0$ when $S_{hcg}=0.0$ is assumed, the estimated R_{CO2} will be low. On the other hand if $S_{hcg}=0.0$ when $S_{hcg} > 0$ is assumed, the estimated R_{CO2} will be high. The error introduced by an incorrect S_{hcg} of 0.02 is approximately 15%.

Using this model, we have assessed the errors caused by incorrect values of the reference parameters, S_w, ϕ, and P_{ref}. The error expressed as a percent of the true value is plotted in Figure 10 for the same R_{CO2} values used in Figure 9. A 15% perturbation of the true reference values were used, which we feel covers the expected variation in these parameters over the inter-well section. The error response as a function of R_{CO2} is approximately symmetric for positive and negative perturbations in the reference parameters used. The assumed S_w has the largest effect, followed by the assumed effective pressure, with the assumed porosity having the smallest effect. Overall, the estimated R_{CO2} is most sensitive to S_{hcg}, since an error of 0.02 in S_{hcg} causes a comparable error of 15% in S_w, but S_{hcg} may vary by more that 0.02.

17
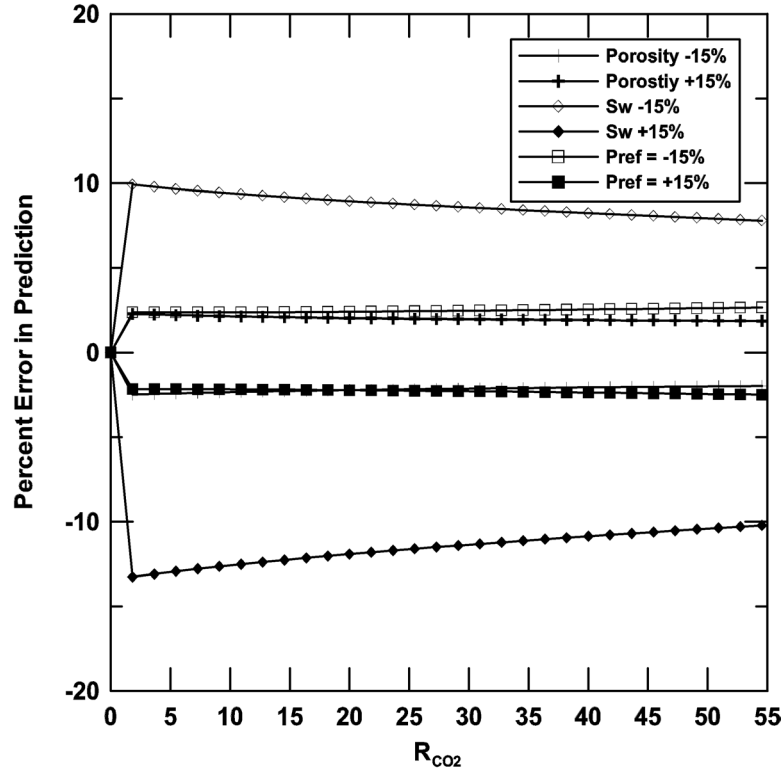
Figure 10. *Error in predicted R_{CO2} as a percentage of the true value. Reference values of porosity (ϕ), water saturation (S_w) and effective pressure (P_{ref}) are in error by +-15%. The 15% range covers the expected variation in these parameters over the inter-well section.*

Figure 11 shows the calculated absolute R_{CO2} (left side) and R_{CO2} expressed as a percent of R_{CO2}^{max} (right side) generated from the geophysical parameter changes shown in Figure 5, using the two-step process described above. Pressure (P) from a history-matched flow simulation model at the beginning of CO_2 injection was used as the reference pressure. The predicted R_{CO2} never reached R_{CO2}^{max}, so no S_{CO2} was needed to account for remaining $-\Delta V_R$. The predicted R_{CO2} shows a strong correlation with the location of perforation intervals (shown as black dots on the green CO_2 hydro-fracture line) that account for the majority of the injected CO_2. The percentage of injected CO_2 going into each perforation in the 11-8WR well (Figure 1) is plotted in the center of Figure 11 and shows that the upper four perforations account for 95% of all the CO_2. Almost 50% of the CO_2 goes into the uppermost perforation. The location of this perforation corresponds with the large $+R_{CO2}$ associated with the fault zone and region above, indicating loss of substantial CO_2 into the upper portions of the reservoir. The second, third, and fourth perforations from the top account for roughly another 45% of CO_2 injected, with each perforation aligning with a laminar zone of $+R_{CO2}$. The only poor correlation between injected CO_2 and predicted $+R_{CO2}$ occurs at the perforation at a depth of 1,850 ft. At this depth, a laminar $+R_{CO2}$ zone aligns with a perforation, but the injectivity log indicates little injected CO_2. A possible explanation for this zone of increased CO_2 is the down-dip CO_2 injector 12-7W. This injector lies along the same

hydraulic fracture azimuth as the 11-8WR (Figure 1) and shows considerable CO_2 injection into the geologic unit that intersects our image plane at 1,850 ft depth.
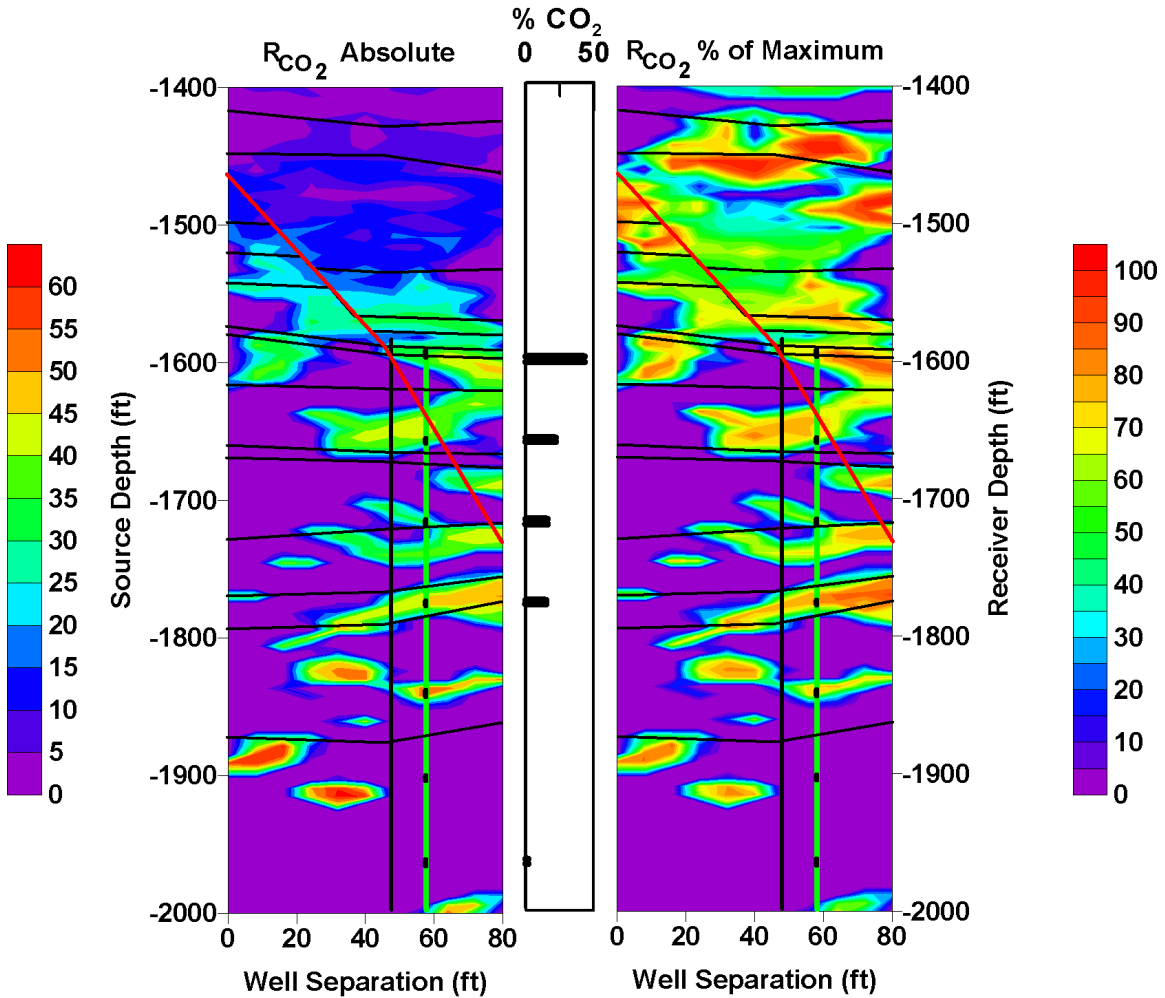
Figure 11. *Predicted CO_2/oil ratio (R_{CO2}). Left side shows absolute R_{CO2}, right side shows R_{CO2} as a percent of the maximum value for the given pressure and temperature. Major unit boundaries are shown as black horizontal lines, estimated location of previous water injection fracture is shown as a vertical black line, estimated location of the CO_2 injection fracture is shown as a vertical green line, perforation intervals for CO_2 injection are shown as black dots on top of the CO_2 injection fracture, and the mapped location of a fault zone is shown as a red diagonal line.*

The upper section of the fault (left side), where geologic unit boundaries are offset correlates with an increase in R_{CO2}, whereas the lower section (right side), where no displacements are mapped, does not. This is consistent with an increased permeability along portions of the fault that have significant movement compared to portions that do not. We interpret this image as indicating that CO_2 from the uppermost perforation is moving up dip along the fault zone and leaking into the high-permeability units above.

The image of R_{CO2} shown in Figure 11 has apparent higher vertical resolution of increased CO_2 zones compared to the geophysical anomalies shown in Figure 5. While there are zones of $-\Delta V_p$ associated with the same perforation intervals correlated with $+R_{CO2}$, there are additional areas of $-\Delta V_p$ above and below that do not correspond to $+R_{CO2}$. Because V_s is insensitive to the fluid substitutions (Figure 7c), we do not expect to see a correlation between ΔV_s and CO_2, either in the gas phase or dissolved in oil. Electrical conductivity changes will be related to changes in oil saturation through the change in S_w; these conductivity changes would also show a correlation to the displacement of water by oil, which may or may not be oil with dissolved CO_2 in it. So, although the $\Delta\sigma$ image (Figure 5) is correlated with the ΔV_p image, it also does not correlate with the injection intervals nearly as well as the derived R_{CO2} image of Figure 11. Overall the R_{CO2} image has higher correlation with the injection intervals than the geophysical change images as well as being more horizontally stratified, as is the permeability structure of the formation.

Conclusions

We have used a roc-properties model, based on a close packing of spherical grains in conjunction with Gassmann's equation, to simulate the relationships between reservoir parameters of the Lost Hills diatomite and seismic compressional and shear velocities. A volumetric mixing law models bulk density. Parameters of the rock-properties model are derived by a simultaneous fitting of compressional velocity and density logs, using a simplex L1-norm minimization, given the observed porosity and fluid-saturation logs as well as measured pressure, temperature, and oil properties. Although the spherical grain model may not ideally represent the microscopic structure of the diatomite, the model accurately predicts the bulk seismic velocities and densities as a function of the fluid saturations, pressure, and porosity as measured by log data and measurements made on core samples. Calculations using the derived rock-properties model show that the rock bulk shear velocity primarily depends on pressure changes, with the effects of water saturation changes on shear velocity being of second order. The calculations also show that the presence of even a small amount of hydrocarbon gas strongly effects the relationships between V_p and the reservoir parameters. The influence of gas on compressional velocity makes it impossible to separate the effects of changes in hydrocarbon gas saturation, CO_2 gas saturation, and the effects on the oil caused by dissolved CO_2 on V_p without additional independent information. Crosswell EM data was used to provide estimates of changes in electrical conductivity that are directly related to changes in water saturation, thus providing an estimate of the change in water saturation that is independent from the seismic data.

To quantitatively predict the location and amount of CO_2 in the crosswell image plane the change of P wave velocity is decomposed into the part that can be predicted by the estimated changes in water saturation and pressure and the part predictable by a change in CO_2 content. The process relies on the assumption that the CO_2 will first dissolve in the oil and will only enter the gas phase after the oil has absorbed the maximum amount of CO_2 possible for the *in situ* pressure and temperature conditions. Using this procedure, we have demonstrated that by combining seismically derived changes in compressional

and shear velocity with EM derived changes in electrical conductivity, estimates of pressure change, water saturation change and CO_2 gas/oil ratio can be made in a complex reservoir containing oil, water, hydrocarbon gas and introduced CO_2. The resulting predicted CO_2 /oil ratio, R_{CO2}, is better correlated with logged unit boundaries than are any of the images of changes in geophysical parameters. The size of the predicted CO_2-rich zones correlate with the amount of CO_2 that enters the formation through each perforation. The predicted ΔR_{CO2} images indicate that a significant portion of the injected CO_2 is filling the upper portions of the section above the intended injection interval. These conclusions are validated by CO_2 injectivity measurements made in the 11-8WR well.

While we have tried to produce quantitative estimates of the CO_2 in place by estimating the CO_2/oil ratio, the values of CO_2/oil ratio depend on our assumptions about the partitioning of CO_2 between oil and gas phase. In addition the assumed values of *in situ* hydrocarbon gas affect the estimates of the CO_2/oil ratio so that the absolute values of our estimates may be in error. The main advantage of the approach described in this paper is the decoupling of the effects of pressure and water saturation changes from those caused by CO_2. This produces the improved spatial correlation between the estimated CO_2/oil ratio and the CO_2 injectivity logs when compared to the geophysical change images.

This analysis relies on many assumptions that were required because the project was not originally designed to use this methodology. In future applications, the number of assumptions could be substantially reduced by design. In particular, considerable benefit could be drawn from repeat logging of the wells with a full suite of logs. This would provide control points for the ΔP, ΔS_w, ΔS_g, ΔV_p, ΔV_s, and $\Delta\sigma$, all of which would serve to greatly constrain the problem. Log measurements of the geophysical parameters would provide information for better starting models, with constraints on the velocity, density, and electrical conductivity at the well locations. Additionally, measurements of S_{CO2} and the amount of CO_2 dissolved in the oil would provide a basis for determining the partitioning of the residual velocity between the two, as well as eliminate the need to assume that all of the CO_2 dissolves in the oil before CO_2 gas is evoked as a mechanism of velocity change.

Acknowledgments

References

Archie, G. E., 1942, The electrical resistivity log as an aid in determining some reservoir characteristics. Trans. Am. Inst. Mech. Eng., **146**, 54-62.

Betzel, M. and Wang, Z., 1992, Seismic properties of pore fluids, Geophys., **57**, 1396-1408.

Bilodeau, B. J., 1995, Determining water saturation in diatomite using wireline logs, Lost Hills Field, California. SPE29653, in Proceedings of the Western Regional SPE Meeting, Bakersfield, CA 1995, 369-382.

Brie, A., Pampuri, F., Marsala, A. F., Meazza, O., 1995, Shear sonic interpretation in gas-bearing sands, SPE30595, in Proceeding of the SPE Annual Technical Conference, Dallas, Tx, 701-710.

Chung, F. T. H., Jones, R. A., Burchfield, T. E., 1988, Recovery of viscous oil under high pressure by CO_2 displacement: A Laboratory Study, SPE 17588, in Proceedings of the SPE Annual Technical Conference, Tianjin,China, 401-410.

Gassmann, F., 1951, Elasticity of porous media: Uber die Elastizitat poroser Medien: Vierteljahrsschrift der Naturforschenden Gesselschaft in Zurich, Heft 1.

Goudswaard, J. C. M., ten Kroode, F. P. E., Snieder, R. K. and Verdel, A. R., 1998, Detection of lateral velocity contrasts by crosswell traveltime tomography, Geophysics, **63**, 523-533.

Hashin, Z., and Shtrikman, S., 1963, A variational approach to the elastic behavior of multiphse materials, J. Mech. Phys. Solids, **11**, 127–140.

Harris, J. M., Nolen-Hoeksema, R. C., Langan, R. T., Van Schaack, M., Lazaratos, S. K., and Rector, J. W., 1995, High-resolution crosswell imaging in a west Texas carbonate reservoir: Part 1- Project summary and interpretation, Geophysics, **60**, 667-681.

Jackson, M. J. and Tweeton, D. R., 1996, 3DTOM: Three-Dimensional Geophysical Tomography, US Dept. of the Interior, Bureau of Mines, Report of Investigation 9617.

Landro, M. 2001, Discrimination between pressure and fluid saturation changes from time-lapse seismic data., Geophysics, **66**, 836-844.

Lazarator, S. K., Harris, J. M., Rector J. W. and Van Schaack, M., 1995, High-resolution crosswell imaging of a West Texas carbonate reservoir: Part 4- Reflection imaging, Geophysics, **60**, 702-711.

Magee, J. W. and Howley, J. A., 1994, A predictive model for the thermophysical properties of carbon dioxide rich mixtures, Research Report RR-136, Gas Processors Association, Tulsa, OK.

Nemeth, T., Normark, E. and Qin, F., 1997, Dynamic smoothing in crosswell traveltime tomography, Geophysics, **62**, 168-176.

Newman, G. A., 1995, Crosswell electromagnetic inversion using integral and differential Equations: Geophysics, **60**, 899-911.

Rector W. J. editor, 1995, Special issue: Crosswell methods, Geophysics, **60**.

Wang, Z., 2001, Personal communication.

Wang, Z., Cates, M. E. and Langan, R. T., 1998, Seismic monitoring of a CO_2 flood in a carbonate reservoir: A rock physics study, Geophysics, **63**, 1604-1617.

Wilt, M. J., Alumbaugh, D. L., Morrison, H. F., Becker, A., Lee, K. H. and Deszcz-Pan, M., 1995, Crosswell electromagnetic tomography: System design considerations and field results, Geophysics, **60**, 871-885.